Purcell effect of nitrogen-vacancy centers in nanodiamond coupled to propagating and localized surface plasmons revealed by photon-correlation cathodoluminescence

Sotatsu Yanagimoto,[1] Naoki Yamamoto,[1] Takumi Sannomiya [1,2,*] and Keiichirou Akiba[1,3,†]

[1]*Department of Materials Science and Engineering, School of Materials and Chemical Technology, Tokyo Institute of Technology, 4259 Nagatsuta, Midoriku, Yokohama 226-8503, Japan*

[2]*JST-PRESTO, 4259 Nagatsuta, Midoriku, Yokohama 226-8503, Japan*

[3]*Takasaki Advanced Radiation Research Institute, National Institutes for Quantum and Radiological Science and Technology, 1233 Watanuki, Takasaki, Gunma 370-1292, Japan*

We measured the second-order correlation function of the cathodoluminescence intensity and investigated the Purcell effect by comparing the lifetimes of quantum emitters with and without metal structure. The increase in the electromagnetic local density of state due to the coupling of a quantum emitter with a plasmonic structure causes a shortening of the emitter lifetime. Since the plasmon-enhanced electric field is confined well below the wavelength of light, the quantum emitter lifetime is changed in the nanoscale range. In this study, we combined cathodoluminescence in scanning (transmission) electron microscopy with Hanbury Brown–Twiss interferometry to measure the Purcell effect with nanometer and nanosecond resolutions. We used nitrogen-vacancy centers contained in nanodiamonds as the emitters and compared their lifetime in different environments: on a thin SiO_2 membrane, on a thick flat silver film, and embedded in a silver film. The lifetime reductions of nitrogen-vacancy centers were observed in the samples with silver. We evaluated the lifetime by analytical calculation and numerical simulations and revealed the Purcell effects of emitters coupled to the propagating and localized surface plasmons.

I. INTRODUCTION

To implement quantum communications and optical computing, the transition probability of a quantum emitter (QE) is one of the speed-limiting factors for the information processing [1–3]. When a QE is coupled to an optical resonator or plasmonic structure, its transition probability can increase, which is called the Purcell effect [4]. Since the coupling between the QE and the nanostructure is sensitive to the nanoscopic geometries, a visualization method of photonic information with nanoscale resolution is required. The Purcell effect can be evaluated by using changes in the lifetime of the QE, which is usually measured with a laser pulse excitation and synchronized detection. Among various proposed QEs, nitrogen-vacancy (NV) emission centers in nanodiamonds (NDs) are considered as a promising candidate featuring highly stable optical properties even at room temperature and functional emission properties for sensing based on electron spins [5,6]. However, the lifetime of ND emitters is strongly dependent on their dielectric environment, i.e., the ND structure itself [7–9], and therefore, it is necessary to measure individual NDs to evaluate the lifetime. To measure the lifetime of individual NDs by fully photon-based methods, they must be separated more than the diffraction limit of light, and nanoscopic measurement of a subwavelength object is not straightforward. Although super-resolution microscopy, such as stochastic optical reconstruction microscopy (STORM) [10] and stimulated emission depletion (STED) microscopy [11,12], is becoming popular, the stochastic approach is not suited for lifetime measurement because it requires temporally resolved detection and the depletion approach could possibly modify the lifetime of the target object due to the scattering of the depletion light by nanostructures.

Besides purely optical means, cathodoluminescence (CL) microscopy, in which the nanoresolution electron beam of a scanning (transmission) electron microscope [S(T)EM] is utilized for the excitation of the light emitters, has been considered as another tool to measure nanoscale optical characteristics [13,14]. The electron beam-based method enables evaluating the optical properties well beyond the diffraction limit of light, and the spatial resolution can go down to subangstrom [15]. A high-resolution structural image can be obtained simultaneously as the CL measurement, which allows direct comparison of the optical and structural information. For instance, localized surface plasmon (LSP) and surface plasmon polariton (SPP) have been visualized at nanoscales by CL [8,16,17]. The lifetime measurement using CL typically requires a large-scale measurement system that integrates a pulsed electron gun as an excitation source [18,19] and a synchronized detector, which is especially complicated for STEM with high acceleration voltages.

As an alternative to using a pulsed electron gun, the lifetime measurement based on the Hanbury Brown–Twiss (HBT) interferometer combined with the STEM/SEM CL has been

---

*sannomiya.t.aa@m.titech.ac.jp
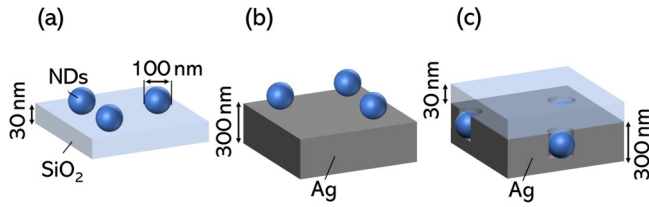
†akiba.keiichiro@qst.go.jp

205418-1

FIG. 1. Schematics of the fabricated samples. The samples were prepared by drop-casting the ND solution onto (a) sample A, a 30-nm-thick SiO_2 membrane and (b) sample B, a 300-nm-thick Ag film on an InP substrate. (c) Sample C is prepared by depositing a 300-nm-thick Ag film on a 30-nm SiO_2 membrane with ND particles on it. All samples were placed on the Cu grid.
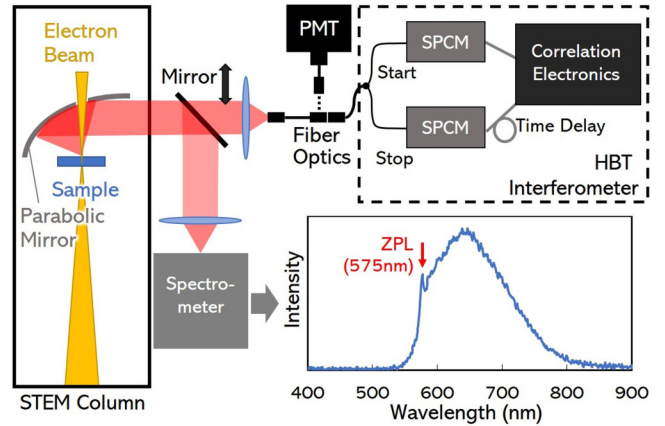

FIG. 2. Schematic illustration of the CL-STEM and optical setup for the HBT measurement. A parabolic mirror collimates the emitted light that is transferred either to a spectrometer, photomultiplier tube (PMT), or HBT interferometer, which is selected by the movable mirror and optical fiber connection. Inset: CL spectrum of an ND without the metal structure (sample A) measured at room temperature with the exposure time of 10 s. The zero-phonon line (ZPL) is indicated by the red arrow.

recently proposed [20–23]. Since HBT-based measurement is a fully passive method that requires modifications only in the light detection system without pulsing the electron source, such a setup can be readily implemented to higher voltage microscopes, like STEM. This type of method has been applied to QEs at low temperatures [20,23] and quantum wells at room temperature [21,24]. The Purcell effect of the coupling between QEs and LSPs has also been evaluated [23,25]. However, using CL-HBT measurement no Purcell effect based on the coupling to propagating SPPs has been experimentally observed [22], while such coupling between a dipole and SPPs is expected [26].

In this paper, we experimentally clarify this controversial coupling of QEs and SPPs with electron beam excitation by comparing the statistical lifetime data of individual NDs using the HBT-based STEM CL. We used NV centers in NDs as a typical candidate of QEs. The lifetime is obtained through photon bunching in the correlation measurement, which can be analytically described with a simple two-level system.

As the simplest coupling system, we first analyze NVs coupled to SPPs on a flat metal surface, and then propose a more efficient coupling of QEs to SPPs and LSPs by embedding NDs in metal films. The Purcell effect based on the coupling between QEs and SPPs or LSPs was experimentally proved with clear shifts in the lifetime histograms of individual NDs. We evaluated the Purcell effect in detail with both analytical and numerical methods providing insights into the coupling dependence on the wavelength, orientation, and location of the emitter dipole.

II. METHOD

A. Sample fabrication

ND solution (900174-5ML, Sigma-Aldrich, America) containing 900 or more NV centers was used. The average diameter of the NDs is 100 nm. Three types of samples (samples A, B, and C) as illustrated in Fig. 1 are prepared. NDs were dispersed on a 30-nm-thick free-standing SiO_2 membrane for sample A and on a 300-nm-thick silver film thermally deposited on an InP substrate for sample B. For sample C, NDs were dispersed on a 30-nm SiO_2 thin membrane, followed by sputter deposition of a 300-nm Ag film to embed the NDs in the Ag film. More fabrication details are shown in the Supplemental Material [27]. In all the measurement, the electron beam is incident and the optical

signal is detected from the upper side in Fig. 1. Sample A without metal was used as a reference to evaluate the lifetime change in samples B and C.

B. Lifetime measurement by CL

The lifetime of the QE $\tau_0[s]$ is the reciprocal of the total decay rate $\gamma_0[s^{-1}]$. The total decay rate can be expressed as a sum of the decay rates due to photon emission (γ_r), absorption into the surrounding environment (γ_n), and plasmon excitation (γ_p),

$$\gamma_0 = \gamma_r + \gamma_n + \gamma_p. \qquad (1)$$

The decay due to plasmon excitation is proportional to the electromagnetic local density of state (EMLDOS) near the QE [1,26,29]. EMLDOS is the number of electromagnetic modes per unit volume coupled with the harmonic oscillating mode of the QE, which increases with the addition of plasmon mode, for example, if there is a metal surface near the QE. The Purcell effect is generally quantified and evaluated by the Purcell factor $F_p = \gamma_0/\gamma_0^{\text{free}}$, where γ_0^{free} is the decay rate in free space [30]. The lifetime τ_0 is obtained by measuring the second-order correlation function $g^{(2)}(\tau)$ using an HBT interferometer [Fig. 2(a)]. $g^{(2)}(\tau)$ is defined by

$$g^{(2)}(\tau) = \frac{\langle I(t)I(t+\tau)\rangle}{\langle I(t)\rangle\langle I(t+\tau)\rangle}, \qquad (2)$$

where $I(t)$ is the CL signal intensity as a function of time t and τ denotes the time delay. The HBT interferometer consists of a system that divides the CL signal into two paths and allows measuring the $g^{(2)}(\tau)$ of the incident photons using single-photon counting modules (SPCMs). We used a CL detection system installed in a STEM (JEM-2000FX, JEOL, Japan) equipped with a thermal emission gun to measure the lifetime of individual NDs, as shown in Fig. 2. The light
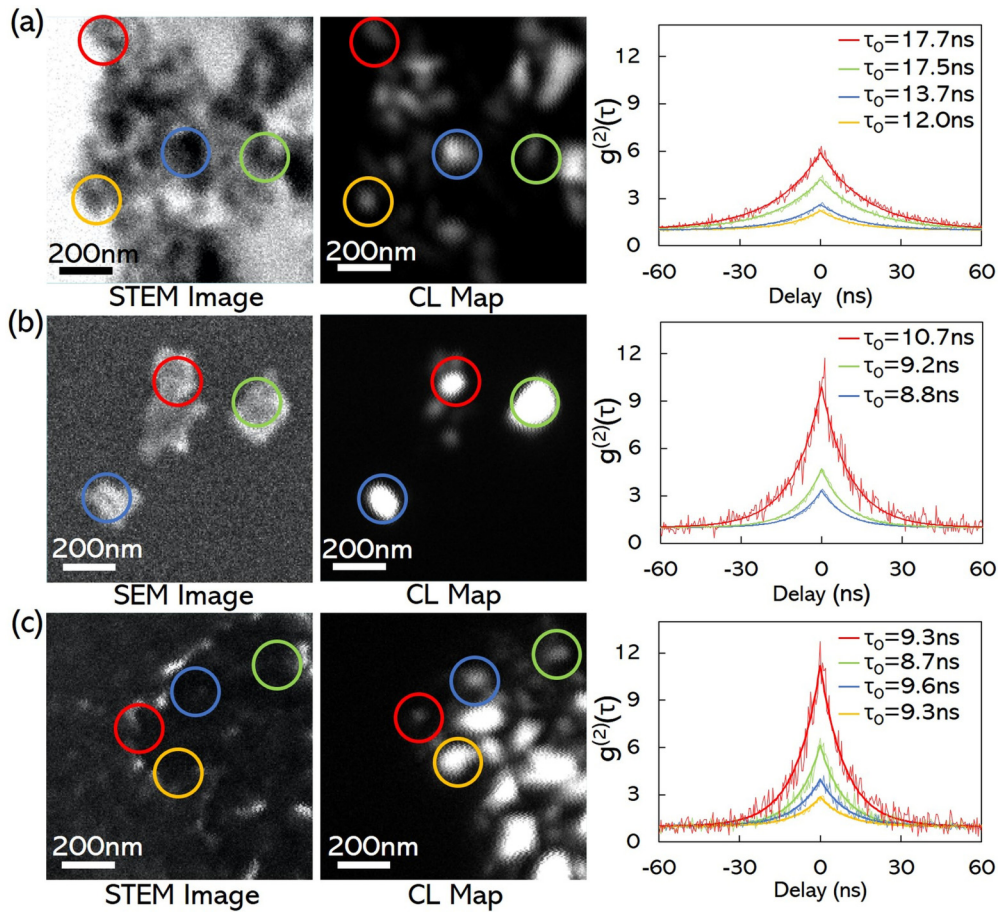
FIG. 3. CL-HBT measurement results of samples (a) A, (b) B, and (c) C, respectively. From left to right: SEM or STEM image, CL panchromatic image, and $g^{(2)}(\tau)$ plots with fitted curves for NDs in each sample. The color of $g^{(2)}(\tau)$ curve in each graph corresponds to the color of the circle in the map indicating the measured NDs.

emitted from the sample is guided out of the STEM column by a parabolic mirror, and transferred either to a spectrometer for CL spectrum measurement, to a photomultiplier tube (PMT) for panchromatic CL mapping, or to the HBT measurement system. The thermal photon radiation from the electron source is avoided in CL detection by letting the direct reflection from the substrate going through the hole of the parabolic mirror for the electron beam path and by subtracting the stray signal as background. The contribution of the thermal photons to $g^{(2)}(0)$ is negligibly small in the $g^{(2)}(\tau)$ measurement and does not affect the lifetime measurement due to the significantly short coherence time [31]. We performed the measurement at room temperature at an accelerating voltage of 80 kV and a beam current of between 17 and 60 pA, which forms a probe of 10 nm or less with the convergence half angle of about 1 mrad. We confirmed that this condition is feasible for the lifetime measurement of NDs to obtain clear bunching features in the $g^{(2)}(\tau)$ correlation curve within 200-s exposure (see Supplemental Material for the current dependence [27]). The CL spectrum from a single ND of sample A without a metallic structure is shown in the inset of Fig. 2. We observed the emission from the NV^0 center, which has a zero-phonon line (ZPL) at a wavelength of 575 nm [6], but without the charged center (NV^-). This result agrees with the previous report [32] that only the emission from NV^0 can be observed

in CL. Thus the $g^{(2)}(\tau)$ measurement using CL in this paper provides information on the lifetime of NV^0 centers in NDs.

III. EXPERIMENTAL RESULTS

Figure 3 shows the SEM or STEM (bright field) images (left panel), CL maps (center panel), and $g^{(2)}(\tau)$ curves (right panel) for representative ND particles in the same field of view for each sample. The selected ND particles are indicated by circles, of which color corresponds to the $g^{(2)}(\tau)$ curve. The experimental lifetime τ_0^{Exp} of each sample was obtained by fitting the correlation plot with $g^{(2)}(\tau) = 1 + A \exp(-\frac{|\tau|}{\tau_0^{\text{Exp}}})$. The coefficient A is equal to $[g^{(2)}(0) - 1]$ and is expressed as follows:

$$g^{(2)}(0) - 1 = \frac{e\xi}{2\eta\tau_0^{\text{Exp}}I_b},\qquad(3)$$

where ξ is the emission fluctuation, η is the excitation probability by one incident electron, and I_b is the electron beam current. This expression of the $g^{(2)}(\tau)$ function can be analytically derived based on the rate equation of a two-level system (see the Supplemental Material [27]). The photon bunching occurs even at room temperature, however, with shorter
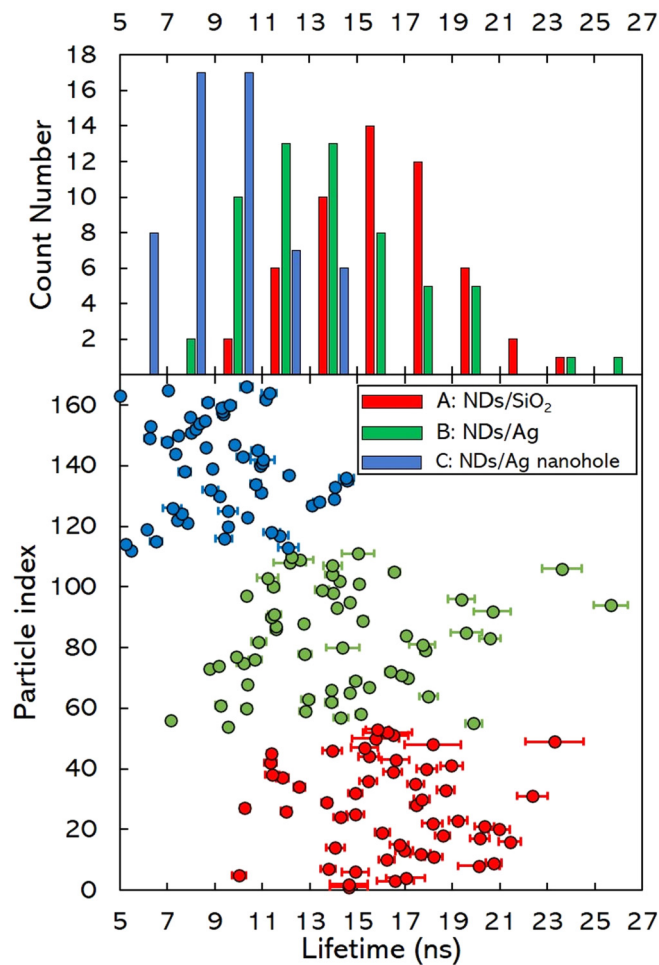
FIG. 4. Histograms (top) and scatter plots (bottom) of the lifetime measurement of sample A (red), B (green), and C (blue). The bin width for the histogram is set to 2 ns. The error bars of individual lifetime measurement are shown in the scatter plot.

lifetimes compared to those under liquid N_2 cooling condition, which is about 20 ns on average [20].

The value of $[g^{(2)}(0) - 1]$ is inversely proportional to the beam current of the incident electron [21]. From this relation between $[g^{(2)}(0) - 1]$ and the beam current, the excitation probability can be deduced, which is shown in the Supplemental Material [27]. Even without the metal structure, the values of $g^{(2)}(0)$ and lifetime of bare NDs in sample A vary significantly from particle to particle. This is due to differences in the shape of the particles, distribution of NV centers within the particles, and the surrounding environment [33,34]. We investigated the size dependence of the Purcell factor using

electromagnetic field simulation and revealed that the Purcell factor can vary by the particle size. The details of this size effect simulation are discussed in the Supplemental Material [27]. In spite of the wide distribution of the lifetime values, we find a trend that the lifetime is shorter and $g^{(2)}(0)$ is larger for samples B and C compared to the bare NDs in sample A. To evaluate this tendency and distribution of the lifetime, we measured 53, 58, and 55 NDs for samples A, B, and C, respectively and made a histogram of the lifetime, as shown in Fig. 4. The lifetime distribution of individual NV particles is presented in the bottom part.

The histogram and scatter plot clearly show that the lifetime distributions with metallic structures (samples B and C) are shifted to shorter lifetime values compared to sample A. The shift was particularly pronounced in sample C. The lifetime distribution originates from the inhomogeneities of the original nanodiamond particles (i.e., shape, size, dipole distribution, and so on), which is supported by the simulated lifetime dependence on the particle size (Supplemental Material Fig. S6 [27]) as well as by the constant lifetime value which is independent of the beam current (Fig. S5 [27]). To statistically and quantitatively confirm the lifetime shift considering the distribution, we performed Wilcoxon-Mann-Whitney statistical U test [35]. This U test is a method of determining the probability that two statistical data are extracted from the same population. If the probability is small enough, it is determined that the shift of the lifetime distribution is not due to statistical fluctuation, but in this case due to the Purcell effect. We run the test at the 5% level of significance and the probability between A-B, B-C, and C-A are calculated to be $p_{AB} = 4.39 \times 10^{-4}$, $p_{BC} = 1.84 \times 10^{-11}$, $p_{CA} = 1.13 \times 10^{-16}$, respectively. All results are well below the significance, meaning a substantial separation of the distributions and justifying the statistical evaluation and comparison of the Purcell effect. Table I shows the Purcell factors calculated from the mean, mode, and median of each sample data. All the statistical values gave the same tendency of the lifetime, and therefore, we used the Purcell factor calculated from the mean for the following discussion. The mean values of the Purcell factor of samples B and C are $F_p^{\text{Exp}B} = 1.15$, and $F_p^{\text{Exp}C} = 1.73$, respectively. These values again verify that the NV centers embedded in metal (sample C) are more affected by the Purcell effect than those on a flat metal substrate (sample B).

We find that the lifetime distribution is narrower for sample C with the shorter lifetime compared to sample A. This tendency of lifetime distribution is related to an additional decay rate, i.e., γ_p, which can be confirmed by modeling a certain decay rate distribution and shifting it by a constant γ_p. The resultant lifetime distribution becomes narrower in the

TABLE I. Lifetime and Purcell factor of different statistical values.

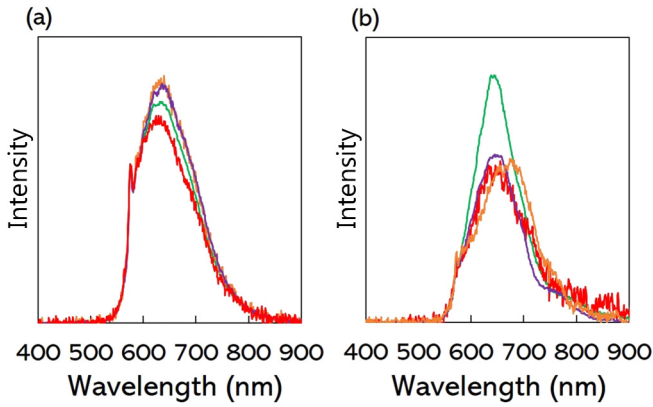| Sample	Mean		Mode		Median	
	Lifetime (ns)	Purcell factor	Lifetime (ns)	Purcell factor	Lifetime (ns)	Purcell factor
A	16.3		16		16.5	
B	14.2	1.15	13	1.23	13.9	1.19
C	9.4	1.73	9	1.78	9.3	1.77

FIG. 5. CL spectra of ND particles of (a) sample A and (b) sample C. The spectra are normalized by the intensity of ZPL at the wavelength of 575 nm.
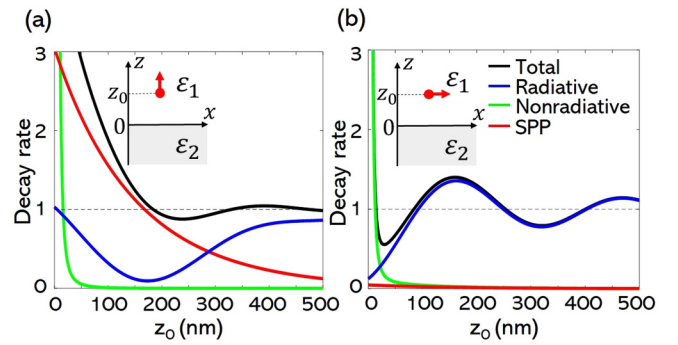

FIG. 6. Normalized decay rate of a dipole in vacuum on a flat Ag surface, analytically calculated as a function of the distance from the surface according to Eq. (4). (a) Vertical (z) and (b) horizontal (x) dipoles placed on the Ag surface (z dipole: $\mu_x = \mu_y = 0$, $\mu_z = 1$; x dipole: $\mu_x = 1$, $\mu_y = 0$, $\mu_z = 0$).

time domain (see the Supplemental Material for details on the change of distribution [27]).

We also notice the tendency that the $g^{(2)}(0)$ values are larger in the samples with metal structures, which are represented by 4.09, 6.93, and 7.11 as mean values for samples A, B, and C under the same excitation condition, respectively. This can be attributed to the increase of γ_0 (or decrease of τ_0) because the $g^{(2)}(0)$ increases with γ_0 [see Eq. (3)]. In addition, the $g^{(2)}(0)$ value may also involve the effect of the secondary electron emitted from supporting materials by electron irradiation: More secondary electrons are expected to be emitted in samples B and C than in sample A since the bulk Ag substrate can produce more secondary electrons than the thin free-standing SiO_2 membrane. The increase of the luminescence intensity in samples B and C can be due to the excitation of the secondary electrons. This may introduce both larger emission fluctuation ξ and excitation probability η [27]. Our result of a large $g^{(2)}(0)$ value with the metal substrate suggests a more dominant fluctuation increase. In the previous study [22], where the excitation electron beam is defocused and hitting predominantly the metal surface, the $g^{(2)}(0)$ value is smaller with the metal. In their case, a large increase in the excitation probability η should be expected, since the direct electron beam irradiation onto the metal surface generates a large number of secondary electrons. This results in the decrease in the $g^{(2)}(0)$ values.

In addition to the lifetime changes, we observed that CL spectrum is also affected by the Purcell effect. Figure 5 shows the representative spectra of ND particles in samples A and C. To compare the shape of the spectrum, we normalized the intensity by the zero-phonon line (ZPL) at the wavelength of 575 nm. The spectral shapes of sample C [Fig. 5(b)] are clearly different from those of sample A [Fig. 5(a)], even though the slight variations are observed in Fig. 5(a). This is consistent with the large lifetime shift of sample C, also indicating the wavelength-dependent Purcell factor due to the coupling to a narrow band mode, i.e., LSP (see Fig. S7 in the Supplemental Material [27] for details). The distribution of the Purcell factor due to the inhomogeneity can account for the fact that the variation in sample C [Fig. 5(b)] is more pronounced than sample A [Fig. 5(a)].

IV. DISCUSSION

A. Coupling of an electric dipole to a flat metal surface

We have experimentally shown the Purcell effect of emitters of NDs coupled to a flat metal surface (sample B). This result is different from the previous report, where no lifetime change was observed for NDs on a flat Ag flake [22], probably because the lifetime distribution of their original NDs is too large, concealing the distribution shift. In this section, we analyze such coupling by considering the simplest model that consists of an electric dipole near a metal surface. We assume a system with two domains, i.e., dielectric (domain 1) and metallic (domain 2) half spaces, and an electric dipole in the dielectric half space. The definitions of the model and the axis coordinate are illustrated in the inset of Fig. 6. The media in both domains are homogeneous, isotropic, and linear. The refractive indices are set to $n_1 = \sqrt{\varepsilon_1}$ and $n_2 = \sqrt{\varepsilon_2}$ for domains 1 and 2 respectively, where ε_i is the relative permittivity of domain i. Here, we set domain 1 as vacuum ($n_1 = 1$) or diamond ($n_1 = 2.42$). For the relative permittivity of domain 2, the literature value of Ag is used [36]. In this model, the Purcell factor of an electric dipole with a dipole moment $\boldsymbol{\mu}$ located at $z = z_0$ is expressed as

$$\frac{\gamma_0^{\text{sub}}}{n_1 \gamma_0^{\text{free}}} = 1 + \frac{\mu_x^2 + \mu_y^2}{|\boldsymbol{\mu}|^2} \frac{3}{4n_1^{\frac{3}{2}}} \int_0^\infty \text{Re}\left\{ \frac{s}{s_z} \left[r_s - s_z^2 r_p \right] e^{2ik_1 z_0 s_z} \right\} ds$$

$$+ \frac{\mu_z^2}{|\boldsymbol{\mu}|^2} \frac{3}{2n_1^{\frac{3}{2}}} \int_0^\infty \text{Re}\left\{ \frac{s^3}{s_z} r_p e^{2ik_1 z_0 s_z} \right\} ds, \quad (4)$$

where the z axis is perpendicular to the surface, and r_s and r_p are the Fresnel reflection coefficients for s and p polarizations, respectively [26]. For convenience, we introduced $s = k_\rho / k_1$ and $s_z = \sqrt{1 - s^2} = k_{z1}/k_1$, where k_ρ is the wave-number component parallel to the interface. The dispersion relation of the SPP on the Ag surface is expressed as $s = \sqrt{\frac{\varepsilon_1 \varepsilon_2}{\varepsilon_1 + \varepsilon_2}}$ ($s = 1$ corresponds to the light line). Therefore, the normalized decay rate due to radiation, absorption, and excitation of the SPP can be separately obtained by integrating Eq. (4) over appropriate ranges of s, and the total of them corresponds to the Purcell factor F_p. Here, we used the integration ranges according to Weber and Eagen [37]. By using Eq. (4), the normalized

TABLE II. Purcell factors of a dipole on a metal surface calculated with the analytical formula.

Domain 1	Purcell factor		
	Horizontal (x) dipole	Vertical (z) dipole	Total
Diamond	1.12	1.34	1.19
Vacuum	0.65	2.87	1.39

decay rates of dipoles in vacuum ($n_1 = 1$) set horizontally and vertically to the interface were calculated at the wavelength of 575 nm as a function of the vertical position of the dipole from the interface z_0, as shown in Fig. 6.

The total decay rate of the dipole is sensitive to the position within the distance of $z_0 < 100$ nm. We notice that the nonradiative decay rate due to absorption to the Ag substrate (green line) does not strongly depend on the direction of the dipole moment and exhibits a monotonous decrease with distance. In contrast, the interference between the radiative field from the dipole and the reflection field from the Ag surface causes oscillating features in the radiative decay rate, which is wavelength dependent. The total Purcell factor converges to 1 at the limit of the infinite separation distance $z_0 \to \infty$. The decay rate due to the SPP excitation γ_{SPP} of the vertical dipole is larger than that of the horizontal dipole at all distances because the vertical dipole can more efficiently excite SPPs by inducing surface charges with the electric field perpendicular to the metal surface.

Photons detected in the HBT experiment have various wavelengths due to the broad spectrum, which must be considered when calculating the Purcell factor. We now assume that the dipoles give the same radiation spectrum as shown in Fig. 2(b) and are homogeneously distributed inside a spherical ND particle. On the basis of this model emulating the experiment, we can calculate the averaged Purcell factors. The average Purcell factor F^{Int} is obtained by averaging the Purcell factors over the wavelength range of the spectrum and the volume (or z position). See the Supplemental Material for more details of the averaging [27].

Since the Purcell factor diverges when $z_0 = 0$ nm, as seen in Fig. 6, we assume a gap of 5 nm between the particle and the substrate. This thickness roughly corresponds to the sum of the typical oxide layer thickness on the Ag surface and the amorphous (or graphitized) layer thickness in ND [27,38,39]. Table II shows the calculated results of the Purcell factors averaged over both wavelength and volume when the dielectric domain is diamond ($n_1 = 2.42$) and vacuum ($n_1 = 1$). In both cases, the total Purcell factor exceeds 1, showing that the total decay rate is enhanced by the presence of the Ag substrate. This analytical evaluation gives ideas of the Purcell effect of a flat metal surface such as the case of sample B although we here do not consider the presence of a dielectric sphere boundary around the dipole in the ND particle.

B. FEM simulations

In this section, we numerically evaluate the Purcell factors of the dipoles in finite-sized dielectric spheres in a more complex environment such as sample C. We performed electromagnetic field simulations with a finite element method
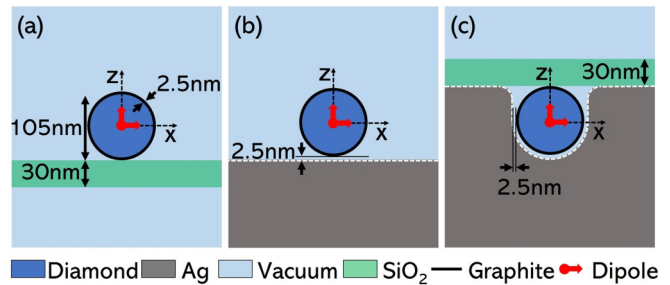

FIG. 7. FEM models. A 100-nm-diameter diamond sphere covered with a 2.5-nm-thick graphite layer is placed (a) on a 30-nm-thick SiO$_2$ membrane (model A), (b) on an Ag substrate (model B), and (c) in an Ag hole with a rounded edge with a radius of curvature of 25 nm [46]. For model C, the Ag hole is covered with a 30-nm-thick SiO$_2$ membrane to emulate sample A. An electric point dipole is placed at the center of the sphere. The results with the excitation electric dipoles in different positions are found in the Supplemental Material [27].

(FEM) using COMSOL Multiphysics and calculated the Purcell factors considering the dielectric effect of the sphere. FEM can also provide electric field distributions, giving insights into EMLDOS and the resonance modes that couple to the emitter dipole [40–42].

Three models, A, B, and C, as shown in Fig. 7, are prepared according to the experiment. The Purcell factors are calculated using model A as a reference and compared with the experimental results. An electric point dipole with a dipole moment $|\boldsymbol{\mu}| = 1$[Cm] is placed in a spherical ND particle with a diameter of 100 nm, and the entire system is surrounded by a perfectly matched layer (PML). In all models, the ND particle is covered by a 2.5-nm-thick graphitized layer, which was experimentally confirmed [27] and also previously reported [39]. The calculation cell size is set to double the wavelength of the radiation field, and the thickness of the PML is set to 60% of the wavelength [40]. Although we have seen the analytical results that the Purcell factor depends on the distance from the substrate as shown in Fig. 6, we here present only dipoles placed in the center of the particle as the representative case. The results of the dipoles at different positions are shown in the Supplemental Material [27]. The wavelength-dependent Purcell factors were calculated for the emitter dipole moments in the z-axis and x-axis directions. The refractive index of diamond was set to 2.4 and the literature values of the dielectric function of Ag [43], graphite [44], and SiO$_2$ [45] were used.

By considering that carbon has poor adhesion to Ag and that the particles used in the experiment are not perfectly spherical [27], it is expected that there is a gap between the Ag substrate and the particle. In addition, an Ag oxide layer covers the surface of the Ag substrate [27,38,39]. Therefore, for models B and C, a 2.5-nm gap between the particle and Ag surface was introduced. This gap helps avoid field singularities at the triple interface points. The Purcell factors were calculated from the FEM results in the following procedure [26,40]. The calculation details are summarized in the Supplemental Material [27].

Figure 8 shows the calculation results of the electromagnetic field simulation with the excitation electric dipole located at the center of the ND particle. The Purcell factor
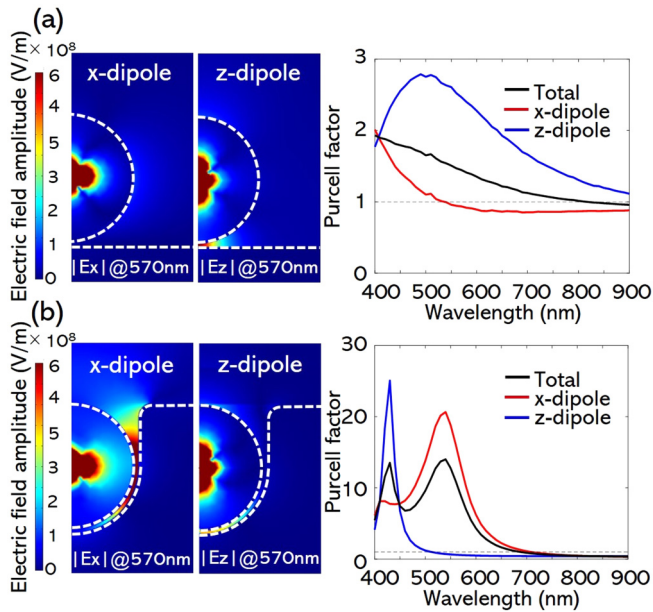
TABLE III. Wavelength-averaged Purcell factors calculated from FEM results.

Model	Purcell factor		
	x dipole	z dipole	Total
B	0.90	2.00	1.66
C	3.90	0.47	3.82

FIG. 8. FEM simulation for (a) model B and (b) model C. From left to right: x-component electric field map with the x-dipole excitation, z-component electric field map with the z-dipole excitation, and the Purcell factor as a function of the wavelength, respectively. The excitation electric dipole is located at the center of the ND particle and the Purcell factor is calculated by integrating the inner product of the excitation dipole moment and the amplitude of the generated electric field. For the mapping, only half of the space is shown, based on the symmetry.

spectra are calculated by volume integration of the inner product of the excitation dipole moment and the amplitude of the generated electric field (see the Supplemental Material [27]). For model B, the electric field is enhanced at the gap between the particle and the substrate, especially for the dipole orientation along the z axis (z dipole). Also, the Purcell factor is larger for the z dipole than for the x dipole. We note that this result is consistent with the analytical calculation of a dipole on a flat metal surface as expressed in Eq. (4). Similar to the analytical calculation, the Purcell factors exhibit a strong dependence on the dipole orientation due to the coupling strength with the structure, i.e., the coupling to SPPs. The spectral response in Fig. 8(a) is indeed similar to the analytical one with a dipole placed 50 nm above the silver surface (see the Supplemental Material [27]).

For model C, as shown in the field maps in Fig. 8(b), the electric field in ND is more enhanced compared to model B. This enhancement of EMLDOS is more remarkable with the x-oriented dipole. Indeed, the calculated Purcell factors are stronger for x-dipole excitation than for z dipole, as shown in Fig. 8(b). We notice the LSP resonance peaks in the spectra: an in-plane mode at 540 nm with x-dipole excitation and an out-of-plane mode at 430 nm with z-dipole excitation. This wavelength dependent Purcell effect is consistent to the experimentally obtained spectral modification for sample C (Fig. 5). Since this model also consists of a continuous metal surface as in model B, the Purcell factor must be derived from both SPP and LSP. Since we were not able to experimentally capture the wavelength dependent Purcell factors due to the limited

emission wavelength range of NV centers, we calculated the spectrally averaged Purcell factors of the presented models average to evaluate the average response over the whole spectral range. The averaged results are shown in Table III. Here, the radiative portion of the weighted average was obtained by integrating the Poynting vector above the substrate at a position sufficiently distant from the dipole (see the Supplemental Material [27]).

The Purcell factor of model C is much higher than that of model B. This is because the LSP mode of the nanohole supports larger EMLDOS in the hole where the emitter is placed, compared to the flat surface with propagating SPPs. In comparison with the experimental Purcell factors of the corresponding structures, namely samples B and C, the simulated values show a qualitative agreement that the emitter embedded in a metal nanohole gives rise to stronger Purcell enhancement. The discrepancy of the absolute factors between the experiment and simulation can be explained by the exact shape difference, more lossy permittivity in the actual NDs, and lossy "gap" instead of pure dielectrics. The shape sensitivity can also be understood from more variations of the spectra in samples B and C compared to sample A. Thus, the numerical analysis by FEM revealed the relation between the Purcell factors and the enhanced EMLDOS by SPP and LSP, elucidating the experimental results.

V. SUMMARY

The $g^{(2)}(\tau)$ measurement of individual NDs utilizing CL photon bunching showed that the lifetime and $g^2(0)$ of ND particles have large distributions. In the presence of a flat metal surface (sample B), the lifetime distribution shifts to short values compared to pristine NDs (sample A). This experimentally proves the Purcell effect due to the coupling of NV centers to SPPs. Such coupling of a dipole emitter to SPPs can be analytically formulated, which shows that the Purcell effect largely depends on the direction of the dipole and the distance from the Ag surface. These results indicate that there is a room to improve the coupling between NV centers and SPPs practically by manipulating the dipole orientation and its distance from the metal substrate. For NDs embedded in Ag nanohole (sample C), NV centers are more strongly affected by the Purcell effect, resulting in even shorter lifetimes with a narrower distribution compared to those on flat metal surfaces (sample B). From the evaluation using FEM simulations, it was found that the resonance peak of the in-plane LSP mode of the Ag nanohole overlaps with the emission spectrum of NV. This causes the stronger Purcell effect based on the coupling to the LSP confined at the Ag nanohole, where EMLDOS is more enhanced. In practice, the dissipated energy portion in generating SPPs can be retrieved and utilized by guiding the

SPPs and converting them to photons, e.g., by using gratings [41].

The presented results and discussion give insights not only into the coupling of NV centers to SPPs and LSPs but also into the photon bunching phenomenon itself, which is unique for the electron beam excitation. Since the electron microscopy-based CL-HBT interferometry allows investigating nanoscale dynamics of excitation and emission [20], the fundamental understandings shown here should be useful to unveil the bizarre light–matter–fast-electron interactions and to further develop this methodology.

[1] D. Englund, D. Fattal, E. Waks, G. Solomon, B. Zhang, T. Nakaoka, Y. Arakawa, Y. Yamamoto, and J. Vučkovíc, Controlling the Spontaneous Emission Rate of Single Quantum Dots in a Two-Dimensional Photonic Crystal, Phys. Rev. Lett. **95**, 013904 (2005).

[2] J. T. Choy, B. J. M. Hausmann, T. M. Babinec, I. Bulu, M. Khan, P. Maletinsky, A. Yacoby, and M. Loňar, Enhanced single-photon emission from a diamond-silver aperture, Nat. Photonics **5**, 738 (2011).

[3] F. A. Inam, M. D. W. Grogan, M. Rollings, T. Gaebel, J. M. Say, C. Bradac, T. A. Birks, W. J. Wadsworth, S. Castelletto, J. R. Rabeau, and M. J. Steel, Emission and nonradiative decay of nanodiamond NV centers in a low refractive index environment, ACS Nano **7**, 3833 (2013).

[4] E. M. Purcell, H. C. Torrey, and R. V. Pound, Resonance absorption by nuclear magnetic moments in a solid, Phys. Rev. **69**, 37 (1946).

[5] C. Kurtsiefer, S. Mayer, P. Zarda, and H. Weinfurter, Stable Solid-State Source of Single Photons, Phys. Rev. Lett. **85**, 290 (2000).

[6] O. A. Shenderova, A. I. Shames, N. A. Nunn, M. D. Torelli, I. Vlasov, and A. Zaitsev, Review article: Synthesis, properties, and applications of fluorescent diamond particles, J. Vac. Sci. Technol. B **37**, 030802 (2019).

[7] J. J. Greffet, J. P. Hugonin, M. Besbes, N. D. Lai, F. Treussart, and J. F. Roch, Diamond particles as nanoantennas for nitrogen-vacancy color centers, arXiv:1107.0502v1.

[8] N. Kawasaki, S. Meuret, R. Weil, H. Lourenço-Martins, O. Stéphan, and M. Kociak, Extinction and scattering properties of high-order surface plasmon modes in silver nanoparticles probed by combined spatially resolved electron energy loss spectroscopy and cathodoluminescence, ACS Photonics **3**, 1654 (2016).

[9] R. Savelev, A. Zalogina, S. Kudryashov, A. Ivanova, A. Levchenko, S. Makarov, D. Zuev, and I. Shadrivov, Control of spontaneous emission rate in luminescent resonant diamond particles, J. Phys.: Conf. Ser. **961**, 012007 (2018).

[10] M. Pfender, N. Aslam, G. Waldherr, P. Neumann, and J. Wrachtrup, Single-spin stochastic optical reconstruction microscopy, Proc. Natl. Acad. Sci. **111**, 14669 (2014).

[11] E. Rittweger, K. Y. Han, S. E. Irvine, C. Eggeling, and S. W. Hell, STED microscopy reveals crystal colour centres with nanometric resolution, Nat. Photonics **3**, 144 (2009).

[12] K. Y. Han, S. K. Kim, C. Eggeling, and S. W. Hell, Metastable dark states enable ground state depletion microscopy of nitrogen vacancy centers in diamond with diffraction-unlimited resolution, Nano Lett. **10**, 3199 (2010).

[13] E. J. R. Vesseur, R. De Waele, M. Kuttge, and A. Polman, Direct observation of plasmonic modes in Au nanowires using high-resolution cathodoluminescence spectroscopy, Nano Lett. **7**, 2843 (2007).

[14] L. F. Zagonel, S. Mazzucco, K. March Tence, R. Bernard, B. Laslier, G. Jacopin, M. Tchernycheva, L. Rigutti, F. H. Julien, R. Songmuang, and M. Kociak, Nanometer scale spectral imaging of quantum emitters in nanowires and its correlation to their atomically resolved structure, Nano Lett. **11**, 568 (2011).

[15] H. Sawada, F. Hosokawa, T. Kaneyama, T. Ishizawa, M. Terao, M. Kawazoe, T. Sannomiya, T. Tomita, Y. Kondo, T. Tanaka, Y. Oshima, Y. Tanishiro, N. Yamamoto, and K. Takayanagi, Achieving 63 pm resolution in scanning transmission electron microscope with spherical aberration corrector, Jpn. J. Appl. Phys. Part 2 **46**, L568 (2007).

[16] K. Takeuchi and N. Yamamoto, Visualization of surface plasmon polariton waves in two-dimensional plasmonic crystal by cathodoluminescence, Opt. Express **19**, 12365 (2011).

[17] D. Vu Thi, T. Ohno, N. Yamamoto, and T. Sannomiya, Field localization of hexagonal and short-range ordered plasmonic nanoholes investigated by cathodoluminescence, J. Chem. Phys. **152**, 074707 (2020).

[18] M. Merano, S. Sonderegger, A. Crottini, S. Collin, P. Renucci, E. Pelucchi, A. Malko, M. H. Baier, E. Kapon, B. Deveaud, and J. D. Ganière, Probing carrier dynamics in nanostructures by picosecond cathodoluminescence, Nature (London) **438**, 479 (2005).

[19] J. P. Renault, B. Lucas, T. Gustavsson, A. Huetz, T. Oksenhendler, E. M. Staicu-Casagrande, and M. Géléoc, Time-resolved cathodoluminescence of DNA triggered by picosecond electron bunches, Sci. Rep. **10**, 5071 (2020).

[20] S. Meuret, L. H. G. Tizei, T. Cazimajou, R. Bourrellier, H. C. Chang, F. Treussart, and M. Kociak, Photon Bunching in Cathodoluminescence, Phys. Rev. Lett. **114**, 197401 (2015).

[21] S. Meuret, T. Coenen, H. Zeijlemaker, M. Latzel, S. Christiansen, S. Conesa-Boj, and A. Polman, Photon bunching reveals single-electron cathodoluminescence excitation efficiency in InGaN quantum wells, Phys. Rev. B **96**, 035308 (2017).

[22] M. A. Feldman, E. F. Dumitrescu, D. Bridges, M. F. Chisholm, R. B. Davidson, P. G. Evans, J. A. Hachtel, A. Hu, R. C. Pooser, R. F. Haglund, and B. J. Lawrie, Colossal photon bunching

in quasiparticle-mediated nanodiamond cathodoluminescence, Phys. Rev. B **97**, 081404 (2018).

[23] H. Lourenço-Martins, M. Kociak, S. Meuret, F. Treussart, Y. H. Lee, X. Y. Ling, H. C. Chang, and L. H. Galvão Tizei, Probing plasmon-NV^0 coupling at the nanometer scale with photons and fast electrons, ACS Photonics **5**, 324 (2018).

[24] S. Meuret, T. Coenen, S. Y. Woo, Y. H. Ra, Z. Mi, and A. Polman, Nanoscale relative emission efficiency mapping using cathodoluminescence $g^{(2)}$ imaging, Nano Lett. **18**, 2288 (2018).

[25] M. Jiang, L. Zheng, Y. Li, H. Shan, C. Chi, Z. Liu, Y. Huang, Z. Dang, F. Lin, and Z. Fang, Tailoring ZnO spontaneous emission with plasmonic radiative local density of states using cathodoluminescence microscopy, J. Phys. Chem. C **124**, 13886 (2020).

[26] L. Novotny and B. Hecht, *Principles of Nano Optics* (Cambridge University Press, Cambridge, UK, 2006).

[27] See Supplemental Material at http://link.aps.org/supplemental/10.1103/PhysRevB.103.205418 for additional details. Supplemental Material includes Ref. [28].

[28] K. Iakoubovskii, K. Mitsuishi, K. Y. Nakayama, and K. Furuya, Mean free path of inelastic electron scattering in elemental solids and oxides using transmission electron microscopy: Atomic number dependent oscillatory behavior, Phys. Rev. B **77**, 104102 (2008).

[29] G. C. D. Francs, J. Barthes, A. Bouhelier, J. C. Weeber, A. Dereux, A. Cuche, and C. Girard, Plasmonic Purcell factor and coupling efficiency to surface plasmons. Implications for addressing and controlling optical nanosources, J. Opt. (Bristol, U. K.) **18**, 094005 (2016).

[30] A. V. Akimov, A. Mukherjee, C. L. Yu, D. E. Chang, A. S. Zibrov, P. R. Hemmer, H. Park, and M. D. Lukin, Generation of single optical plasmons in metallic nanowires coupled to quantum dots, Nature (London) **450**, 402 (2007).

[31] D. B. Scarl, Measurements of photon correlations in partially coherent light, Phys. Rev. **175**, 1661 (1968).

[32] M. Solà-Garcia, S. Meuret, T. Coenen, and A. Polman, Electron-induced state conversion in diamond NV centers measured with pump-probe cathodoluminescence spectroscopy, ACS Photonics **7**, 232 (2020).

[33] L. H. G. Tizei and M. Kociak, Spectrally and spatially resolved cathodoluminescence of nanodiamonds: Local variations of the NV^0 emission properties, Nanotechnology **23**, 175702 (2012).

[34] L. H. G. Tizei and M. Kociak, Spatially Resolved Quantum Nano-Optics of Single Photons Using an Electron Microscope, Phys. Rev. Lett. **110**, 153604 (2013).

[35] R. Bergmann and J. Ludbrook, Different outcomes of the Wilcoxon—Mann—Whitney test from different statistics packages, Am. Stat. **54**, 72 (2000).

[36] E. D. Palik, *Handbook of Optical Constants of Solids* (Academic Press, New York, 1985).

[37] W. H. Weber and C. F. Eagen, Energy transfer from an excited dye molecule to the surface plasmons of an adjacent metal, Opt. Lett. **4**, 236 (1979).

[38] N. Yamamoto, S. Ohtani, and F. J. García De Abajo, Gap and Mie plasmons in individual silver nanospheres near a silver surface, Nano Lett. **11**, 91 (2011).

[39] O. A. Shenderova and G. E. McGuire, Science and engineering of nanodiamond particle surfaces for biological applications (review), Biointerphases **10**, 030802 (2015).

[40] Y. Chen, T. R. Nielsen, N. Gregersen, P. Lodahl, and J. Mørk, Finite-element modeling of spontaneous emission of a quantum emitter at nanoscale proximity to plasmonic waveguides, Phys. Rev. B **81**, 125431 (2010).

[41] I. Bulu, T. Babinec, B. Hausmann, J. T. Choy, and M. Loncar, Plasmonic resonators for enhanced diamond NV^- center single photon sources, Opt. Express **19**, 5268 (2011).

[42] H. Siampour, S. Kumar, and S. I. Bozhevolnyi, Nanofabrication of plasmonic circuits containing single photon sources, ACS Photonics **4**, 1879 (2017).

[43] S. Babar and J. H. Weaver, Optical constants of Cu, Ag, and Au revisited, App. Opt. **54**, 477 (2015).

[44] B. Kwiecinska, D. G. Murchison, and E. Scott, Optical properties of graphite, J. Microsc. **109**, 289 (1977).

[45] J. Kischkat, S. Peters, B. Gruska, M. Semtsiv, M. Chashnikova, M. Klinkmüller, O. Fedosenko, S. MacHulik, A. Aleksandrova, G. Monastyrskyi, Y. Flores, and W. T. Masselink, Mid-infrared optical properties of thin films of aluminum oxide, titanium dioxide, silicon dioxide, aluminum nitride, and silicon nitride, Appl. Opt. **51**, 6789 (2012).

[46] C. S. Perera, K. C. Vernon, and A. McLeod, Simulations of the spontaneous emission of a quantum dot near a gap plasmon waveguide, J. Appl. Phys. **115**, 054314 (2014).